

Accurate equivalent circuit model for millimetre-wave UTC photodiodes

Michele Natrella,¹ Chin-Pang Liu,¹ Chris Graham,¹ Frederic van Dijk,² Huiyun Liu,¹ Cyril C. Renaud,¹ and Alwyn J. Seeds^{1,*}

¹UCL Electronic and Electrical Engineering, Torrington Place, London WC1E 7JE, UK

²III-V Laboratory, 1, Avenue Augustin Fresnel, RD128 F-91767 Palaiseau Cedex, France

*a.seeds@ucl.ac.uk

Abstract: We present a comprehensive study of uni-travelling carrier photodiode impedance and frequency photo-response supported by measurements up to 110 GHz. The results of this investigation provide valuable new information for the optimisation of the coupling efficiency between UTC-PDs and THz antennas. We show that the measured impedance cannot be explained employing the standard junction-capacitance/series-resistance concept and propose a new model for the observed effects, which exhibits good agreement with the experimental data. The achieved knowledge of the photodiode impedance will allow the absolute level of power emitted by antenna integrated UTCs to be predicted and ultimately maximised.

©2016 Optical Society of America

OCIS codes: (250.0250) Optoelectronics; (230.5170) Photodiodes; (350.4010) Microwaves; (040.2235) Far infrared or terahertz; (130.5990) Semiconductors.

References and links

1. H. Eisele, "State of the art and future of electronic sources at terahertz frequencies," *Electron. Lett.* **46**(26), S8–S11 (2010).
2. C. Mann, "Practical challenges for the commercialisation of terahertz electronics," in *IEEE MTT-S International Microwave Symposium Digest* (IEEE, 2007), paper 1705–1708.
3. A. J. Seeds, M. J. Fice, K. Balakier, M. Natrella, O. Mitrofanov, M. Lamponi, M. Chtioui, F. van Dijk, M. Pepper, G. Aeppli, A. G. Davies, P. Dean, E. Linfield, and C. C. Renaud, "Coherent terahertz photonics," *Opt. Express* **21**(19), 22988–23000 (2013).
4. T. Ishibashi, S. Kodama, N. Shimizu, and T. Furuta, "High-speed response of uni-traveling-carrier photodiodes," *Jpn. J. Appl. Phys.* **36**(10), 6263–6268 (1997).
5. H. Ito, S. Kodama, Y. Muramoto, T. Furuta, T. Nagatsuma, and T. Ishibashi, "High-speed and high-output InP-InGaAs unitraveling-carrier photodiodes," *IEEE J. Sel. Top. Quantum Electron.* **10**(4), 709–727 (2004).
6. T. Nagatsuma, H. Ito, and T. Ishibashi, "High-power RF photodiodes and their applications," *Laser Photonics Rev.* **3**(1-2), 123–137 (2009).
7. A. Beling, Z. Li, Y. Fu, H. Pan, and J. C. Campbell, "High-power and high-linearity photodiodes," in *IEEE Photonic Soc. 24th Annual Meeting* (IEEE, 2011), pp. 19–20.
8. H. Ito, T. Furuta, S. Kodama, and T. Ishibashi, "InP/InGaAs uni-travelling-carrier photodiode with 310 GHz bandwidth," *Electron. Lett.* **36**(21), 1809–1810 (2000).
9. C. C. Renaud, D. Moodie, M. Robertson, and A. J. Seeds, "High output power at 110 GHz with a waveguide Uni-travelling carrier photodiode," in *Conf. Proc. - Lasers Electro-Optics Soc. Annu. Meet.* (2007), pp. 782–783.
10. H. Ito, T. Nagatsuma, A. Hirata, T. Minotani, A. Sasaki, Y. Hirota, and T. Ishibashi, "High-power photonic millimetre wave generation at 100 GHz using matching-circuit-integrated uni-travelling-carrier photodiodes," *IEEE Proc. Optoelectron.* **150**, 138–142 (2003).
11. H. Ito, F. Nakajima, T. Furuta, and T. Ishibashi, "Continuous THz-wave generation using antenna-integrated uni-travelling-carrier photodiodes," *Semicond. Sci. Technol.* **20**(7), S191–S198 (2005).
12. C. Renaud, M. Robertson, D. Rogers, R. Firth, P. Cannard, R. Moore, and A. Seeds, "A high responsivity, broadband waveguide uni-travelling carrier photodiode," *Proc. SPIE* **6194**, 61940C (2006).
13. H. J. Song, K. Ajito, Y. Muramoto, A. Wakatsuki, T. Nagatsuma, and N. Kukutsu, "Uni-travelling-carrier photodiode module generating 300 GHz power greater than 1 mW," *IEEE Microw. Wirel. Compon. Lett.* **22**(7), 363–365 (2012).
14. E. Rouvalis, C. C. Renaud, D. G. Moodie, M. J. Robertson, and A. J. Seeds, "Continuous wave terahertz generation from ultra-fast InP-based photodiodes," *IEEE Trans. Microw. Theory Tech.* **60**(3), 509–517 (2012).
15. T. Ishibashi, Y. Muramoto, T. Yoshimatsu, and H. Ito, "Uni-traveling-carrier photodiodes for terahertz applications," *IEEE J. Sel. Top. Quantum Electron.* **20**(6), 79–88 (2014).
16. J. Dyson, "The equiangular spiral antenna," *IRE Trans. Antennas Propag.* **7**(2), 181–187 (1959).

17. R. DuHamel and D. Isbell, "Broadband logarithmically periodic antenna structures," *IRE Int. Conv. Rec.* **5**, 119–128 (1957).
18. J. D. Kraus, R. J. Marhefka, and A. S. Khan, *Antennas for All Applications*, 3rd ed. (Tata McGraw-Hill, 2010).
19. J. Li, B. Xiong, C. Sun, D. Miao, and Y. Luo, "Analysis of frequency response of high power MUTC photodiodes based on photocurrent-dependent equivalent circuit model," *Opt. Express* **23**(17), 21615–21623 (2015).
20. E. Rouvalis, M. Chtioui, M. Tran, F. van Dijk, M. Fice, C. Renaud, G. Carpintero, and A. Seeds, "High-speed uni-travelling carrier photodiodes for InP photonic integrated circuits," *Opt. Express* **20**, 9172–9177 (2012).
21. E. Rouvalis, C. C. Renaud, D. G. Moodie, M. J. Robertson, and A. J. Seeds, "Traveling-wave Uni-Traveling Carrier photodiodes for continuous wave THz generation," *Opt. Express* **18**(11), 11105–11110 (2010).
22. M. Natrella, E. Rouvalis, C.-P. Liu, H. Liu, C. C. Renaud, and A. J. Seeds, "InGaAsP-based uni-travelling carrier photodiode structure grown by solid source molecular beam epitaxy," *Opt. Express* **20**(17), 19279–19288 (2012).
23. A. J. Seeds, C. Renaud, and M. Robertson, "Photodetector including multiple waveguides," United States patent US7851782 (B2) (2010).
24. G. Lucovsky, M. E. Lasser, and R. B. Emmons, "Coherent Light Detection in Solid-State Photodiodes," *Proc. IEEE* **51**(1), 166–172 (1963).
25. R. P. Riesz, "High speed semiconductor photodiodes," *Rev. Sci. Instrum.* **33**(9), 994–998 (1962).
26. H. Kroemer, "Heterostructure bipolar transistors and integrated circuits," *Proc. IEEE* **70**(1), 13–25 (1982).
27. H. Kroemer, "Heterostructure bipolar transistors: What should we build," *J. Vac. Sci. Technol. B* **1**, 126–130 (1983).
28. R. L. Anderson, "Experiments on Ge-GaAs heterojunctions," *Solid-State Electron.* **5**(5), 341–351 (1962).
29. A. A. Grinberg, M. S. Shur, R. J. Fischer, and H. Morkoc, "An investigation of the effect of graded layers and tunneling on the performance of AlGaAs/GaAs heterojunction bipolar transistors," *IEEE Trans. Electron Dev.* **31**(12), 1758–1765 (1984).
30. V. Ryzhii and M. Shur, "Tunnelling- and barrier-injection transit-time mechanisms of terahertz plasma instability in high-electron mobility transistors," *Semicond. Sci. Technol.* **17**(11), 1168–1171 (2002).
31. A. Rumiantsev, P. Sakalas, N. Derrier, D. Celi, and M. Schroter, "Influence of probe tip calibration on measurement accuracy of small-signal parameters of advanced BiCMOS HBTs," in *2011 IEEE Bipolar/BiCMOS Circuits Technol. Meet. (BCTM)* (IEEE, 2011), pp. 203–206.
32. A. J. Lord, "Comparing the accuracy and repeatability of on-wafer calibration techniques to 110GHz," in *29th Eur. Microwave Conf.* (1999), 28–31.
33. K. Kurishima, H. Nakajima, T. Kobayashi, Y. Matsuoka, and T. Ishibashi, "Fabrication and characterization of high-performance InP/InGaAs double-heterojunction bipolar transistors," *IEEE Trans. Electron Dev.* **41**(8), 1319–1326 (1994).
34. T. Ishibashi, T. Furuta, H. Fushimi, and H. Ito, "Photoresponse characteristics of uni-traveling-carrier photodiodes," *Proc. SPIE* **4283**, 469–479 (2001).
35. T. Ishibashi, N. Shimizu, and S. Kodama, "Uni-traveling-carrier photodiodes," *Tech. Dig. Ultrafast Electron. Optoelectron.* **13**, 83–87 (1997).
36. R. K. Ahrenkiel, R. Ellingson, S. Johnston, and M. Wanlass, "Recombination lifetime of $\text{In}_{0.53}\text{Ga}_{0.47}\text{As}$ as a function of doping density," *Appl. Phys. Lett.* **72**(26), 3470–3472 (1998).

1. Introduction

Interesting potential applications are envisaged within the THz gap (100 GHz – 10 THz), such as spectroscopic sensing, broadband wireless communications and imaging for both medical and security purposes. For such applications to be possible, compact, tuneable and power-efficient Continuous-Wave (CW) sources operating at room temperature need to be realised [1–3]. Antenna integrated photomixers are promising candidates for the development of such sources. A photomixer employed for this purpose is the Uni-Travelling Carrier Photodiode (UTC-PD) [4,5], whose implementation based on InP materials is an established solution for CW terahertz generation via photomixing of lasers operating at 1550 nm. The photo-response of the UTC-PD is dominated by the electron transport in the whole structure. This is an essential difference from the conventional pin PD, where both electrons and holes contribute to the response, and the low-velocity hole-transport dominates the performance. In UTCs electrons exhibit velocity overshoot ($3\text{--}5 \times 10^7$ cm/s) in the carrier collection layer [4]; in addition the UTC-PD generates higher output saturation current even in the high-frequency operation due to the reduced space charge effect in the depletion layer, which also results from the high electron velocity in the depletion layer [6]. These properties make the UTC-PD a high speed and high output power photodiode [7–14]. Since its invention in 1997 [4], modified UTC-like structures with a hybrid absorber have been developed, to optimise the bandwidth and responsivity [15]. All of the structures consist of narrow-gap absorbers sandwiched by wide-gap p- and n-contact layers. In this paper we analyse photodiodes having a classical UTC epitaxial structure.

Current research on antenna integrated UTC-PDs is focused on enhancing the emitted power and bandwidth. Emitted power and bandwidth depend on 4 key factors: 1) optical fibre-to-chip coupling efficiency; 2) photodiode bandwidth and optical responsivity; 3) photodiode-to-antenna coupling efficiency; 4) antenna directivity and radiation efficiency. Point 3 (photodiode-to-antenna coupling efficiency) has not received much attention in the literature.

To optimise the efficiency of power coupling between UTCs and antennas, complex-conjugate matching needs to be realised. Therefore it is essential to know the real part (resistance) and imaginary part (reactance) of the UTC output impedance over the frequency range. Design of antennas to integrate with UTCs should take the complex (i.e. not real) nature of the source (UTC) impedance into account in order to realise broadband matching. When the source impedance is real, reflection-less matching with the load (antenna) is equivalent to maximum transfer of power matching (i.e. complex-conjugate matching) and hence, reducing the reflection coefficient automatically leads to maximising the transfer of power from the source to the antenna. For these reasons, on the assumption of driving antennas with a real impedance source, the antenna bandwidth in terms of efficiency of power coupling with the source, can be defined in terms of reflection coefficient ρ , or S_{11} in dB or VSWR (Voltage Standing Wave Ratio) with typical specifications requiring $\rho < 0.2$ $\Rightarrow S_{11} < -14$ dB \Rightarrow VSWR < 1.5 . Antennas like the equiangular spiral and the toothed log-periodic, often integrated with UTCs, have been demonstrated to have constant impedance over a broad frequency range [16–18]. For this reason they can provide broadband matching to a constant impedance driving source. When these antennas are driven by UTC-PDs, such a broadband matching is harder to achieve since the UTC impedance is not constant, with a particularly frequency dependent reactive component.

Recently an experimental and circuit analysis up to 40 GHz, of a back-illuminated modified UTC (MUTC), has been presented in [19] in which the authors discuss a new circuit model to fit the measured S_{11} and show the agreement between measurement and calculation on Smith Charts. In [19] the new circuit model is employed to study the MUTC dynamic frequency response; the transit time contribution to the photo-response is inferred by fitting the measured photo-response, starting from the RC limited response calculated by means of the circuit parameters obtained by fitting the measured S_{11} .

We present a comprehensive study of UTC-PD impedance and frequency photo-response, carried out using experimental techniques up to 110 GHz and a semi-analytical circuit analysis. The device impedance and S_{11} have been measured up to 110 GHz and the frequency photo-response up to 67 GHz. A detailed analysis is performed to find out why the classical diode circuit model, based on the junction-capacitance/series-resistance concept, cannot explain the experimental data, especially in the lower frequency range (DC to 30 GHz) where parasitic effects are negligible and hence cannot be referred to explain the disagreement. A new circuit model is proposed, to explain the observations, that achieves very good agreement with the measurements at all frequencies; a link is suggested between the additional energy storage circuit elements present in the new circuit and quantum mechanical effects taking place between the UTC absorption and collection layers (i.e. through the spacer layers). We also carried out an estimation of the quasi-field generated in the absorber of the analysed UTCs by the graded doping profile, in order to take the transit time limited response into account. The knowledge of the UTC-PD complex impedance up to high frequency, along with accurate antenna design, can enable the prediction and optimisation of the power radiated by antenna integrated UTC-PDs, not only in terms of trend over the frequency range but even of absolute level of emitted power.

The circuit model we introduce is applicable up to frequencies at which the device dimensions become significant relative to the effective wavelength. For the analysis we present, the model is successfully applied up to 110 GHz, where the effective wavelength is about 70 times greater than the UTC length. The lumped element analysis can be employed up to about 400 GHz, where the effective wavelength is 20 times the UTC length; however to validate the model up to such frequencies the support of 3D full-wave modelling of the whole

UTC structure will be needed. Above 400 GHz the lumped element analysis is expected gradually to lose validity.

2. Device measurement and circuit analysis

The waveguide UTCs characterised in this paper have been provided by III-V Lab; their epitaxial layer structure [20] is shown in Table 1. The UTC epitaxial structure is based on that designed at University College London (UCL) [21–23]. The structure of Table 1 was designed to be monolithically integrated with other components, such as lasers and semiconductor optical amplifiers. To facilitate this, a thick ridge layer of p-doped InP was grown between the p-contact and the absorber layers.

Table 1. Layer structure of the UTCs provided by III-V Lab [20].

Doping (cm^{-3})	Material	Function	Thickness (nm)
p++	GaInAs	p-contact	200
p+	InP	Ridge Layer	1000
p-gradual	$\text{In}_{0.53}\text{Ga}_{0.47}\text{As}$	Absorber	120
n	Q	Spacer layer	–
n	Q	Spacer layer	–
n	InP	Depletion	300
n+	$\text{Q}_{1,17}$	Waveguide	300
n+	InP	n – contact	600
Fe	SI - InP	Substrate	–

The device geometry is the same as the UCL waveguide UTCs discussed in [9,12,23]. The photodiodes are integrated with coplanar waveguide contact patterns for the use of air coplanar probes. All the measurements discussed in the paper were carried out at a constant temperature of 22 °C, maintained by means of a Peltier Cooling Module and a temperature controller.

2.1 S_{11} and impedance measurement and circuit analysis

The UTC S_{11} and impedance measurement was performed up to 110 GHz in two steps, covering the sub-ranges 10 MHz to 67 GHz and 75 GHz to 110 GHz. In the lower frequency range (10 MHz to 67 GHz) an Agilent performance network analyser (PNA) was employed, directly capable of operating from 10 MHz up to 67 GHz. The device was probed using a Cascade air coplanar probe with coaxial electrical connection. A one port short-open-load-through (SOLT) calibration was performed up to the probe tips, by means of a Cascade impedance standard substrate (ISS). For measurements in the W-band (75 GHz to 110 GHz), an Agilent extender (mixer) was connected to the PNA, enabling operation between 75 GHz and 110 GHz. In this range a Cascade air coplanar probe with a waveguide electrical connection (WR10/WG27) was used. In this frequency range the one port SOLT calibration was performed by means of a Cascade W-band impedance standard substrate.

The UTC S_{11} (relative to the 50 Ω PNA impedance) magnitude in dB and phase in degrees are displayed in Fig. 1, while the impedance real part (resistance) and imaginary part (reactance), both in Ohm, are given in Fig. 2. Devices with 3 x 15 μm^2 and 4 x 15 μm^2 area were characterised, at 0 V and 2 V reverse bias; repeatability and reliability of these experimental results were confirmed by performing the measurements on several different devices for each size. We plot the results in a Cartesian system as this will allow a clear comparison between measured and numerical results, especially in the lower frequency range (DC to 30 GHz) where, as mentioned previously, parasitic effects cannot be used to explain any potential disagreement. As expected, the device reactance exhibits a capacitive behaviour (i.e. is negative) within the measured frequency range and is larger (in absolute value) for smaller area devices; applied negative bias also slightly increases the reactance absolute value. The impedance real part is visibly larger for smaller devices.

The theoretical capacitance for the two different area devices at zero bias, assuming the relative electrical permittivity for the depletion layer InP to be 12.5 and ignoring the effect of the two spacers, should be 16.6 fF for the 3 x 15 μm^2 UTC and 22 fF for the 4 x 15 μm^2 . On

the other hand, if we try to extract the capacitance C from the measured device reactance $X(f)$, as $C = -1/2\pi fX(f)$, we obtain the curves displayed in Fig. 3. The imaginary part of the impedance is in general a combination of capacitive and inductive components. However, at lower frequencies, the inductive components are much less significant. It follows that in the lower frequency range the curves in Fig. 3 represent the total UTC capacitance.

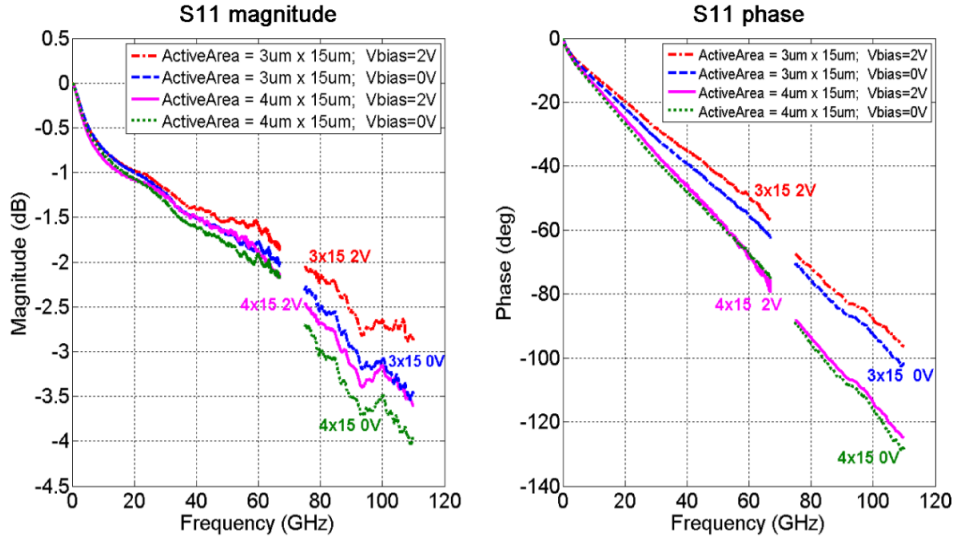


Fig. 1. Measured S_{11} magnitude (dB) and phase (degrees), relative to the PNA 50 Ω impedance.

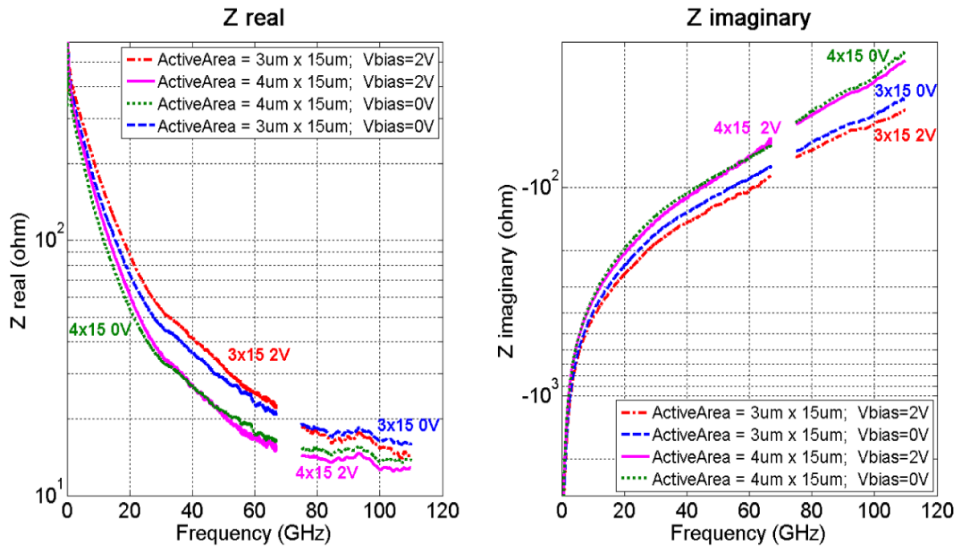


Fig. 2. Measured UTC impedance real part (resistance) and imaginary part (reactance).

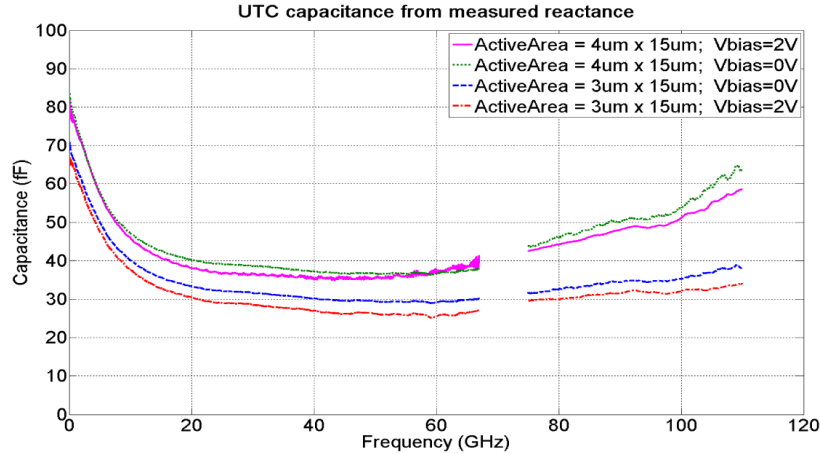


Fig. 3. UTC capacitance derived from the measured device reactance.

A simplified circuit model [24,25], shown in Fig. 4(a), comprising the device depletion capacitance and series resistance, has been commonly adopted as a model for the UTC-PD. A slightly more accurate circuit version, illustrated in Fig. 4(b), includes the resistance R_p across the depletion layer (which is not infinite but in the range of hundreds of $k\Omega$) and also the parasitic capacitance C_p and inductance L_p , whose effect becomes relevant at high frequencies. The arrow in the circle, displayed in the left hand side of both circuits in Fig. 4, is a current source which is only active when the device is illuminated, otherwise it is an open as in the case of the S_{11} /impedance measurement discussed in this section. In any case, in agreement with [19], we found that, when the DC photocurrent is below the saturation, the circuit parameters do not change with respect to the optical power.

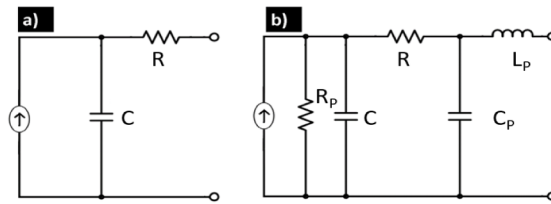


Fig. 4. (a) Simplified circuit model for a photodetector. (b) Simplified circuit model including the large resistance R_p across the depletion layer and also the parasitic capacitance C_p and inductance L_p .

If the UTC capacitance was only due to the single capacitance associated with the depletion layer, one should expect the photodiode capacitance to be essentially frequency independent. In fact, if we consider the circuit in Fig. 4(b), excluding C_p and L_p , the capacitance extracted from the impedance reactance has the expression shown in (1):

$$C_{TOT} = \frac{1}{4\pi^2 f^2 R_p^2 C} + C \quad (1)$$

Equation (1) comprises a frequency dependent term and a constant term (C). C_{TOT} converges to the constant value C very fast, as the frequency f increases; also, the larger the value of C and R_p the faster the convergence. For instance, even for a conservative value of 10 $k\Omega$ for R_p and a value of C as small as that calculated theoretically (16.6 fF), the frequency dependent term in (1) would be already less than 1% of C at 1 GHz. Clearly, for the circuit in Fig. 4(a), C_{TOT} is constant since R_p is infinite. Consequently, the photodiode capacitance would be essentially frequency independent, however this does not seem to be supported by the experimental results shown thus far.

The measured capacitance in Fig. 3 seems to be reasonably constant within the frequency range 20 GHz to 67 GHz. The increasing capacitance values exhibited above 75 GHz are most likely caused by parasitic effects that start to become significant. To the contrary the strongly frequency dependent behaviour displayed below 20 GHz, does seem to suggest a change in the total device capacitance and indeed cannot be explained by means of the traditional single junction capacitance. If the device reactance actually depended only on the junction capacitance, the curves in Fig. 3 should be flat over the whole frequency range below the frequencies affected by parasitic effects. Device capacitance measurements are normally performed at a single frequency, typically below 1 MHz; as can be seen in Fig. 3, the capacitance measured near the lowest frequency handled by the PNA (i.e. 10 MHz) ranges from about 65 fF to more than 80 fF. To verify these low frequency capacitance values, the UTC S_{11} were re-measured using an Agilent network analyser operating from 9 KHz up to 8.5 GHz which provided results consistent with the PNA results (10 MHz to 67 GHz).

Furthermore, the measured device S_{11} and impedance, shown in Figs. 1 and 2, cannot be explained by either of the circuits illustrated in Fig. 4. In order to support this assertion we performed a numerical parameter optimisation to fit the experimental results, sweeping a vast range of values of R , R_p , C and even including C_p and L_p , however the discrepancy is substantial and no satisfactory agreement could be achieved. In Fig. 5 we show how the S_{11} and impedance, of the circuit in Fig. 4(b), change as the depletion capacitance C ranges from 2 fF to 108 fF, and how they compare to the measurements for the $3 \times 15 \mu\text{m}^2$ UTC at zero bias. The parasitic capacitance C_p and inductance L_p are here neglected, the resistance R_p across the depletion layer is taken into account with a value of 300 k Ω (considering its value as infinite would cause the real part of the impedance to be just a constant value); the resistance R is set to 15 Ω , which is the device series resistance. A simultaneous good agreement between impedance real and imaginary part (or equivalently between S_{11} magnitude and phase) cannot be achieved. For instance, when C is equal to 28 fF, measured and calculated impedance imaginary parts are in good agreement, but the real parts are greatly different; on the other hand, when C is equal to 2 fF, measured and calculated impedance real parts exhibit a fair agreement, but the difference between the imaginary parts is very significant. The results shown in Fig. 5 strongly suggest that the difference between measured and calculated response is substantial, and this is particularly noticeable in the trend of the impedance real part up to 50-60 GHz and the S_{11} magnitude up to 20-30 GHz, where C_p and L_p have negligible effect.

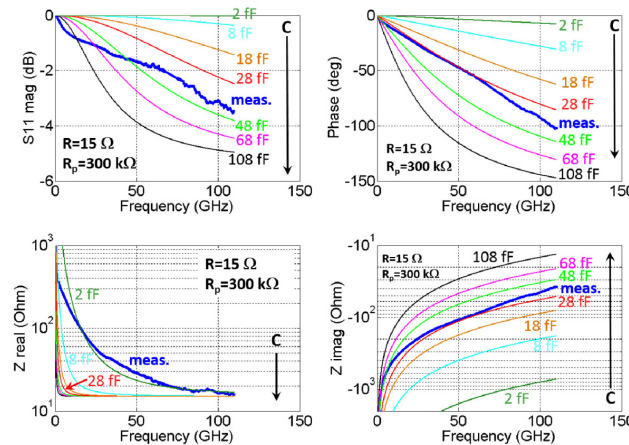


Fig. 5. Comparison between S_{11} /impedance measured for the $3 \times 15 \mu\text{m}^2$ UTC at zero bias and calculated with the circuit in Fig. 4(b), as the depletion capacitance C ranges from 2 fF to 108 fF. The parasitic capacitance C_p and inductance L_p are here neglected, the resistance R_p across the depletion layer is taken into account with a value of 300 k Ω . The resistance R is set to 15 Ω , which is the device series resistance.

A simplified mathematical explanation of this discrepancy can be obtained by considering the analytical expression of the reflection coefficient S_{11} for the circuit in Fig. 4(b), without C_p and L_p . If we consider such a reflection coefficient as a function of the complex variable $s = \sigma + j2\pi f$ (where j is the imaginary unit and f is the frequency) we obtain the expression in (2):

$$S_{11}(s) = \frac{(R - R_0) \left(s + \frac{R + R_p - R_0}{(R - R_0)R_p C} \right)}{(R + R_0) \left(s + \frac{R + R_p + R_0}{(R + R_0)R_p C} \right)} \quad (2)$$

R_0 is the 50 Ω reference impedance. Equation (2) shows that the reflection coefficient is endowed with one pole and one zero, both of the first order. The pole and the zero are equal to (3) and (4):

$$s_{pole} = -\frac{R + R_p + R_0}{(R + R_0)R_p C} \quad (3)$$

$$s_{zero} = -\frac{R + R_p - R_0}{(R - R_0)R_p C} \quad (4)$$

Let us consider two specific values of capacitance C , e.g. 16.6 fF (theoretical value) and 68 fF (measured value at low frequency), as Circuit 1 and Circuit 2 illustrated in Fig. 6.

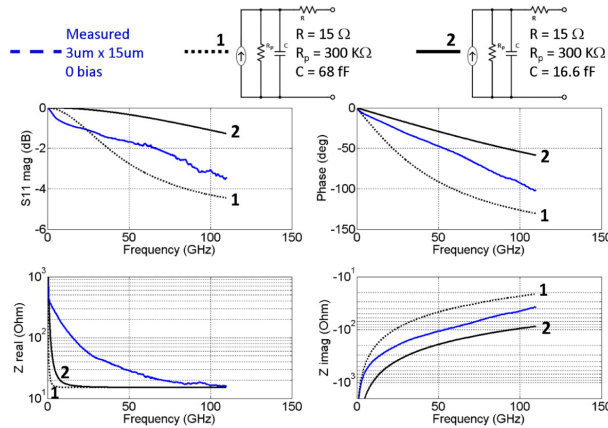


Fig. 6. Comparison between measured S_{11} /impedance of a $3 \times 15 \mu\text{m}^2$ area UTC and S_{11} /impedance obtained from the simplified equivalent circuit for two different values of device capacitance.

The pole is real and negative and corresponds, at steady state, to a frequency of 36 GHz for Circuit 1 and 147.5 GHz for Circuit 2; the zero is real and positive and corresponds to a frequency of 66.9 GHz for Circuit 1 and 274.5 GHz for Circuit 2. As known from circuit theory and control theory, the asymptotic effect of a negative pole of the first order is to produce a 20dB/decade magnitude falloff and a 90° phase decrease, while a positive zero generates a 20dB/decade magnitude increase but still a 90° phase decrease. It follows that both Circuit 1 and 2 would settle, asymptotically, on a flat magnitude and a -180° phase. The S_{11} of Circuit 1 and 2 is hence shaped by S_{pole} and S_{zero} . Circuit 2 S_{11} magnitude starts flatter than Circuit 1, reflecting the fact that Circuit 2 has a pole corresponding frequency four times larger than Circuit 1. In Circuit 1 the pole is located at quite a low frequency (36 GHz) and its effect on the magnitude decrease (which asymptotically would lead to a 20 dB/decade falloff) is already observable, followed by the effect of the zero, at 66.9 GHz, which tends to counterbalance the pole effect and would restore, asymptotically, the magnitude to a flat

trend. The measured S_{11} magnitude, plotted in Fig. 6 as a blue line, exhibits an early decrease, even more pronounced than Circuit 1 however, unlike Circuit 1, it is soon restored to a less steep slope maintaining which it reaches -3.5 dB at 110 GHz; the measured S_{11} phase decreases virtually in a linear fashion down to -100° at 110 GHz.

The only way for the magnitude of a one-pole-one-zero function, such as the S_{11} of Circuit 1 and 2, to fit the measured S_{11} magnitude within the low frequency range (i.e. 0 GHz to 25 GHz), would be to have the pole located at a very low frequency (less than the 36 GHz shown for Circuit 1) and the zero closely following the pole at a slightly higher frequency, like the plot in Fig. 7. Firstly, it has to be noted that, in order to have the pole and the zero located in this way, an unrealistically large capacitance $C = 550$ fF and an unlikely small resistance $R = 3 \Omega$ have to be employed. Secondly, having the pole and the zero both located at such low frequencies, causes the superposition of their asymptotic effects to be already nearly noticeable below 110 GHz, with the S_{11} magnitude settling on a constant value of about -1 dB and the phase on -180° . As a consequence the discrepancy between circuit and measured magnitude becomes more and more considerable above circa 25 GHz, while the discrepancy between circuit and measured phase is substantial over the whole frequency range.

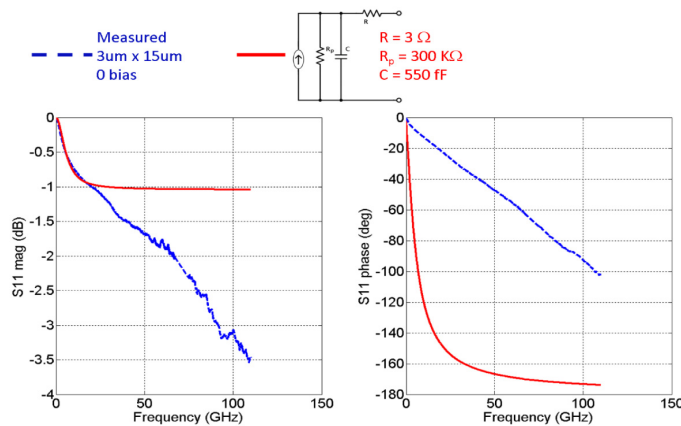


Fig. 7. Example of a one-pole-one-zero function, such as the S_{11} of Circuit 1 and 2, fitting the measured S_{11} magnitude within the low frequency range (i.e. 0 GHz to 25 GHz). In order to have the pole and the zero located in this way, an unrealistically large capacitance $C = 550$ fF and an unlikely small resistance $R = 3 \Omega$ have to be employed.

It seems reasonable to infer and conclude that more poles and zeroes, i.e. a higher order circuit, are necessary in S_{11} to achieve a satisfactory agreement between the measured S_{11} and the circuit-model response.

For the circuit S_{11} function to have more poles and zeroes (i.e. the circuit order to increase), additional independent energy storage elements, such as capacitors and/or inductors, must be introduced. The presence of these new elements though, needs to be justified and a reasonable connection to the device structure and physics has to be suggested. The capacitance C and the resistance R_p in the simplified circuit described in Figs. 6 and 7, essentially account for the effect of the depletion layer, modelled as an appropriate capacitance in parallel with a very large resistance; the rest of the device structure is simply taken into account by the resistance R which includes the resistive effect of the ohmic contacts and the doped layers contributing to the device series resistance. The spacer layers, grown between the absorber and the carrier collection layer, have the function of alleviating the conduction band discontinuity generated at the heterojunction between the narrow band-gap InGaAs and the wide band-gap InP. The electrons move by diffusion within the p-doped absorber layer and, once injected into the carrier collection layer, drift towards the cathode layer with overshoot velocity. The conduction band discontinuity tends to hinder the electron injection into the depletion layer and hence acts as a barrier for the electron transport. The

issue concerning the presence of an offset in the conduction band edge was identified for Heterostructure Bipolar Transistors (HBT), where such a discontinuity gave rise to a barrier impeding the injection of electrons from the emitter into the base region [26,27]; a description was proposed, for the electron transport across this barrier, using a thermionic model discussed by Anderson [28]. A study regarding the effect of graded layers and tunnelling on the performance of AlGaAs/GaAs heterojunction bipolar transistors was presented by Grinberg et al [29]. Here HBTs with an abrupt emitter-base junction and graded HBTs were modelled, using a thermionic-diffusion model, and the electron current density across the heterointerface was calculated together with the electron concentrations at each side of the heterointerface. It was found that the values of the common emitter current gain in HBTs with an abrupt emitter-base junction are smaller than graded HBT because the electron injection is limited by the interface spike barrier. Grinberg also proposed a new thermionic field-diffusion model including the effect of electron tunnelling near the peak of the interface spike and showed that tunnelling effects play an essential role in HBTs with abrupt spikes, while are less important in HBTs with graded junctions. Also, the transit-time effect of the electrons injected from the channel into the gate layer, in a heterostructure similar to a high-electron mobility transistor, was studied theoretically in [30] and it was found that the electron injection depended on the band offset at the heterointerface and occurred via either tunnelling through the top of the barrier or thermionic emission over the barrier.

Based on the above mentioned studies [26–30] it is clear how tunnelling and thermionic emission are the phenomena governing the electron transport across conduction band offsets. As seen in [29], such electron transport is associated with different charge concentrations at each side of the barriers and with possible impediment to the electron passage caused by the potential barrier. Here we suggest the hypothesis that these effects may be reflected, at a macroscopic scale, in a way that can be interpreted as capacitive and resistive effects on the UTC frequency behaviour. In the new Circuit 3, illustrated in Fig. 8, the two spacers have been modelled as two RC parallel circuits (R_2C_2 and R_3C_3), which provide the required additional poles/zeroes in the S_{11} function; the neutral region of the heavily p-doped 120 nm thick absorber is ignored as it would only provide a negligible resistive effect. The R_4C_4 parallel represents the carrier collection layer, while R_1 takes into account the resistive effects of doped materials and ohmic contacts. The parasitic capacitance and inductance C_p and L_p mainly have the function to refine the agreement with the experimental data above 75 GHz. The parasitic inductance L_p is principally due to the coplanar waveguide contact pads, deposited to enable the use of air coplanar probes. It is noted that for the case of the circuit proposed in [19], the presence of an additional independent capacitance (i.e. apart from the capacitance which typically takes the collection layer into account) is justified by the fact that the device under study is a modified UTC (MUTC), in which part of the absorber is undoped.

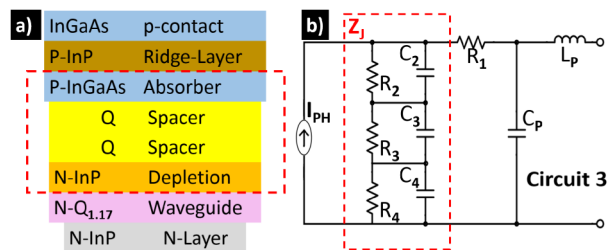


Fig. 8. (a) UTC layer structure. (b) New equivalent circuit, showing the relation with the UTC structure. The two spacers have been modelled as two RC parallel circuits (R_2C_2 and R_3C_3). The neutral region of the heavily p-doped 120 nm thick absorber only provides a negligible resistive contribution. The R_4C_4 parallel represents the carrier collection layer, while R_1 takes into account the resistive effects of doped materials and ohmic contacts. C_p and L_p account for parasitic capacitance and inductance respectively.

Figure 9 shows the comparison between S_{11} /impedance of the new circuit illustrated in Fig. 8 and S_{11} /impedance of a $3 \times 15 \mu\text{m}^2$ area UTC measured at zero bias; all of Circuit 3

elements have been optimised to match the response of the $3 \times 15 \mu\text{m}^2$ area UTC and their optimum values are also displayed in Fig. 9. The agreement between Circuit 3 and experimental results is excellent, also in the lower frequency range (i.e. below 30 GHz) and supports the hypothesis proposed above, regarding the role played by spacer layers and conduction band discontinuities in the photodiode frequency response. If we consider that the value of R_I is bound to be similar to the measured series resistance, the value of R_d has to be very large and the values of the parasitic components C_p and L_p have to be small, then the combination of the remaining parameters providing such an excellent agreement is essentially unique.

Remarkably, to obtain a good agreement between Circuit 3 and the measured S_{11} /impedance of a $4 \times 15 \mu\text{m}^2$ area UTC (still at zero bias) it is not necessary to repeat an optimisation process, but is sufficient to scale down the optimum resistances of the $3 \times 15 \mu\text{m}^2$ UTC by a factor $3/4$ and scale up the capacitances by a factor $4/3$; this comparison is shown in Fig. 10. It is worth noting that the resistance R_I , of $4 \times 15 \mu\text{m}^2$ UTCs, will be slightly larger than $(3/4) \times 15 \Omega$, since only the contributions to the series resistance due to the materials in the ridge actually do scale down by a factor $(3/4)$, but the contribution due to n-contact layer and n-ohmic contact do not.

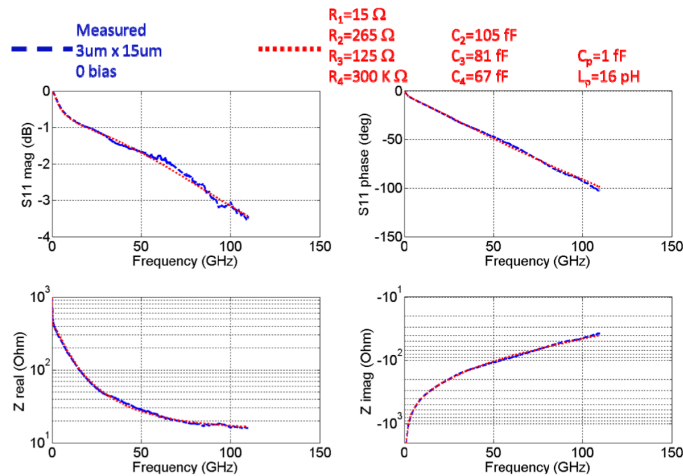


Fig. 9. Comparison between measured S_{11} /impedance of a $3 \times 15 \mu\text{m}^2$ area UTC at 0 V bias (dashed blue line), and S_{11} /impedance obtained from Circuit 3 which models the proposed effect of spacer layers and conduction band discontinuities (dotted red line).

In order to match the experimental results of the $3 \times 15 \mu\text{m}^2$ area UTC measured at 2 V reverse bias, the values of the capacitances C_2 , C_3 , and C_4 , associated with the spacers and the depletion layer, have been adjusted, while all the resistances are unchanged with respect to the 0 V bias case. In particular this is consistent with the fact that the applied voltage should not influence the device series resistance. The agreement is good and depicted in Fig. 11.

As in the zero bias case, for the measurements taken at 2 V reverse bias it is sufficient to scale the optimum resistances and capacitances found for the $3 \times 15 \mu\text{m}^2$ UTC, in order to obtain a good match between Circuit 3 and the measured S_{11} /impedance of the $4 \times 15 \mu\text{m}^2$ area UTC, as illustrated in Fig. 12.

It is noted that, although our $3 \times 15 \mu\text{m}^2$ UTC circuit model contains a 105 fF capacitance, the total device capacitance is in agreement with the measured capacitance (< 70 fF). For the circuit in Fig. 7, the 550 fF capacitance C coincides with the circuit total capacitance, which should also be reflected in the measured capacitance. For this reason the value of 550 fF in Fig. 7 was deemed as unrealistic.

We investigated the effect of the CPW pads on the S_{11} both experimentally and using full-wave modelling. We found that the CPW pads have no or small effect on the measured S_{11} below 67 GHz, whereas they start having a relevant effect in the W-band. De-embedding the

effect of the CPW pads is important in view of the UTC to antenna matching optimisation since the impedance seen from the terminals of an antenna integrated with the UTC does not include the CPW pads. The value of 16 pF for L_p essentially has resulted from the need to fit Circuit 3 S_{11} to the S_{11} measured between 75 GHz and 110 GHz. However, the S_{11} measured in the W-band is affected by the effect of the CPW. Also, uncertainty in the SOLT calibration on wafer at these frequencies may well be non-negligible [31,32]; our measurement in the W-band are likely affected by an inductive error as can be seen in the phase trend, which exhibits a slight offset down with respect to measurement below 67 GHz. The refined value of 7 pF for L_p , found after de-embedding the CPW by means of full-wave modelling, is intrinsic to the UTC geometry and still provides very good agreement with the measurements up to 67 GHz. In the W-band this reduced value of L_p mainly causes the S_{11} phase to decrease less steeply and the impedance reactance to increase less steeply.

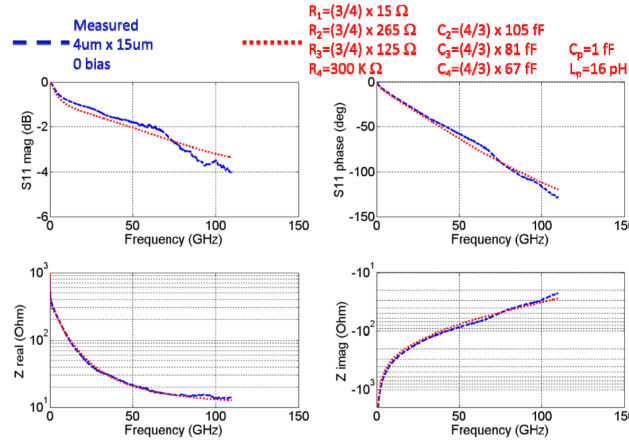


Fig. 10. Comparison between measured S_{11} /impedance of a $4 \times 15 \mu\text{m}^2$ area UTC at 0 V bias (dashed blue line), and S_{11} /impedance obtained from Circuit 3 (dotted red line). The optimum resistance and capacitance values are obtained by scaling the optimum values found for the $3 \times 15 \mu\text{m}^2$ area UTC at 0 V.

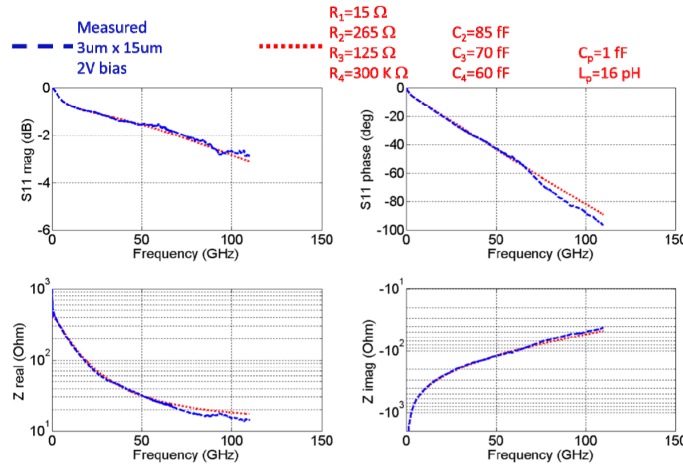


Fig. 11. Comparison between measured S_{11} /impedance of a $3 \times 15 \mu\text{m}^2$ area UTC at 2 V reverse bias (dashed blue line), and S_{11} /impedance obtained from Circuit 3 (dotted red line). The capacitances C_2 , C_3 and C_4 , associated with the spacers and the depletion layer, have been adjusted, while all the resistances are unchanged with respect to the 0 V bias case.

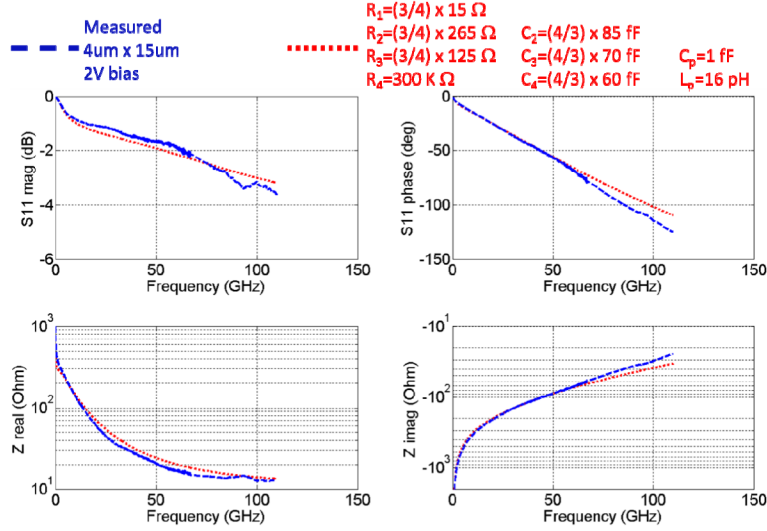


Fig. 12. Comparison between measured S_{11} /impedance of a $4 \times 15 \mu\text{m}^2$ area UTC at 2 V reverse bias (dashed blue line), and S_{11} /impedance obtained from Circuit 3 (dotted red line). The optimum resistance and capacitance values are obtained by scaling the optimum values found for the $3 \times 15 \mu\text{m}^2$ area UTC at 2 V reverse.

2.2 Frequency photo-response measurement and circuit analysis

The UTC frequency photo-response was measured from 10 MHz to 67 GHz by means of an Agilent lightwave component analyser (LCA), based on the performance network analyser (PNA) used for the S_{11} measurements. The optical power set in the LCA was 6 dBm (or 5.6 dBm if measured at the output of the lensed fibre). The measured DC photocurrent was very similar for both devices, namely $460 \mu\text{A}$ for the $3 \times 15 \mu\text{m}^2$ UTC and $490 \mu\text{A}$ for the $4 \times 15 \mu\text{m}^2$ UTC, which therefore exhibited DC responsivities of 0.127 A/W and 0.135 A/W respectively, at a $1.55 \mu\text{m}$ wavelength.

Circuit 3, shown in Fig. 8, can be employed to predict the frequency response of the two different area UTCs and make a comparison with the measured photo-response. For this purpose, the current generator I_{PH} , that was an open-circuit for the S_{11} /impedance evaluation, is now active and accounts for the photocurrent I_{PH} generated by the incident optical power; also, the terminals at which the S_{11} and the impedance were evaluated, are now terminated in a 50Ω load R_L representing the LCA input impedance, to which the RF power generated by the UTC is delivered. If we indicate with Z_J the total impedance associated with absorber, spacers and depletion layer, given by (5) and highlighted in Fig. 8, then we can quantify the relationship between I_{PH} and I_L as in (6).

$$Z_J = \frac{R_2}{1 + j2\pi f R_2 C_2} + \frac{R_3}{1 + j2\pi f R_3 C_3} + \frac{R_4}{1 + j2\pi f R_4 C_4} \quad (5)$$

$$I_L = I_{PH} \frac{Z_J}{(Z_J + R_1)(1 - 4\pi^2 f^2 L_p C_p + j2\pi f R_L C_p) + j2\pi f L_p + R_L} \quad (6)$$

If the amplitude of the current I_{PH} is regarded as constant over the frequency range, the normalised squared modulus of $I_L(f)$ in (6) represents the UTC RC limited relative photo-response. For a comprehensive calculation of the device photo-response, the transit-time effect must be taken into account. The amplitude of the current I_{PH} is not constant over the frequency range but suffers from a decrease caused by the electron transit time across absorber and depletion region. In-depth studies of InP/InGaAs heterojunction bipolar transistors (HBT) have demonstrated that electrons can drift at overshoot velocities, as high as

4×10^7 cm/s [33]; for the 300 nm thick InP collection layer of the UTCs characterised in this paper, such velocity yields a 0.75 ps transit time. However, in a classical UTC structure, for reasonable values of the depletion layer thickness, the transit time across the collection layer is shorter than across the absorber and therefore, the device transit time limited 3 dB bandwidth is mainly determined by the response in the absorption layer. The general expression for I_{PH} was calculated in [4,34,35]. When the doping in the absorber is adequately high ($>$ mid $10^{17}/\text{cm}^3$) [4,34] the holes respond within the dielectric relaxation time $\tau_R = \epsilon/\sigma$ (where ϵ and σ are the material electrical permittivity and conductivity respectively) which for p-InGaAs 10^{18} cm^{-3} can be as short as 33 fs [4]. Under these conditions, the influence of the absorber holes on the UTC bandwidth can be ignored and the device transit-time limited response will only depend on the electron injection current at the absorber/depletion interface and on the transfer function through the collection layer. If no quasi field is present in the absorber, the minority electrons within this layer only move by diffusion and, despite the high mobility of the minority electrons (greater than $4000 \text{ cm}^2/\text{Vs}$ for p-InGaAs 10^{18} cm^{-3}), the transit time across the absorption layer can still be longer than the hole transit time across an equally thick depletion layer in a PIN photodiode [4]. It was shown in [4,35] that the effect of a quasi-field within the absorption layer can be significant when high-mobility InGaAs is used and the transit time limited frequency response can be improved substantially, since the quasi-field helps the electrons to be swept out from the layer. A quasi-field can be generated either via band-gap grading or doping grading, the latter being the case for the UTCs analysed in this paper. To calculate the transit-time frequency response of the UTCs, the contribution of the quasi-electric field generated by the graded doping needs to be taken into account. In compositionally non-uniform semiconductor materials the quasi-electric field acting on the electrons is due to the spatial variation of the electron affinity. For instance, a graded bandgap in the p-absorber of a UTC, decreasing from the p-contact side towards the collector, would generate a quasi-field accelerating the electrons towards the collection layer. In materials with graded doping, as is the case for the p-type absorption layer of our UTCs, the quasi-field is self-induced and accelerates the electrons towards decreasing doping levels; graded doping also produces a gradual bandgap shrinkage that slows down the carrier, however this effect is minor. It has been reported [15] that exponentially graded doping with a variation of two orders of magnitude, for example, can produce 120-meV potential change (no bandgap shrinkage included). The results discussed in [35] show that a quasi-field equivalent to a 50 mV potential can increase the 3 dB bandwidth of a UTC with 120 nm thick absorption and depletion layers, from 160 GHz (diffusion only) to almost 400 GHz; the UTCs we analyse have a 120 nm thick absorber and a 300 nm thick depletion layer, hence their transit time limited 3 dB bandwidth would increase from almost 160 GHz (diffusion only) to over 300 GHz under the effect of the same 50 mV potential. We estimate that the overall potential generated in our UTCs by the graded doping should be in the range 10 mV to 20 mV, enhancing the transit-time limited bandwidth to between 200 GHz and 300 GHz.

Figure 13 illustrates the transit time limited response of a UTC with a 120 nm thick InGaAs absorber and a 300 nm thick InP collection layer, calculated using the equations discussed in [4,34,35] and the estimated quasi-field contribution, for five different scenarios. The continuous red line represents the response due only to the transfer function through the collector, which shows a 3 dB bandwidth of over 500 GHz. The dotted blue line is the transit-time limited response for the pure diffusion case, when no quasi-field is present, and exhibits a 3 dB bandwidth of 152 GHz. The three dashed green lines 1, 2 and 3 represent three possible transit-time limited responses obtained with the contribution of the estimated overall potential (between 10 mV and 20 mV) generated by the doping grading, and have 3 dB bandwidths of about 200 GHz, 235 GHz and 270 GHz respectively. A summary of the parameters employed to calculate the responses in Fig. 13, is given in Table 2. The electron diffusive constant was calculated using the Einstein relation for the diffusion of charged particles. The transit-time limited responses plotted in Fig. 13 can now be used to assess the overall photo-response of our UTCs, incorporating both the RC-limited and transit-time limited contributions. Essentially the ideal current source I_{PH} in Eq. (6) can now be replaced

with a current source whose squared modulus decreases over the frequency range following the responses plotted in Fig. 13. The total frequency response of the $3 \times 15 \mu\text{m}^2$ and the $4 \times 15 \mu\text{m}^2$ UTCs, for diffusion only and the three different quasi-field scenarios shown in Fig. 13, is plotted in Figs. 14 and 15 respectively and compared with the measured photo-response.

Table 2. Summary of the parameters employed to calculate the responses in Fig. 13.

Parameter	Description	Value
W_A	Absorption layer thickness	120 nm
W_C	Collection layer thickness	300 nm
τ_c	Electron transit time across the collection layer, calculated assuming an overshoot velocity of 4×10^7 cm/s [33]	0.75 ps
D_e	Diffusion constant of electrons in the absorber calculated for an electron mobility of $4000 \text{ cm}^2/(\text{Vs})$ [4,35]	$103 \text{ cm}^2/\text{s}$
v_{TH}	Thermionic emission velocity used as a boundary condition at the absorption/collection layer interface	2.5×10^7 cm/s [34,35]
τ_{rec}	Carrier recombination lifetime in the absorber	2 ns [36]

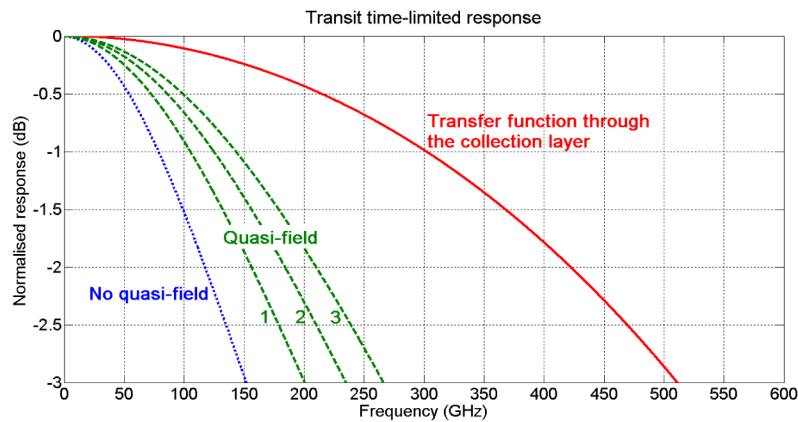


Fig. 13. Transit-time limited response of a UTC with a 120 nm thick InGaAs absorber and a 300 nm thick InP collection layer. The continuous red line represents the decrease due only to the transfer function through the collector. The dotted blue line is the transit-time limited response when no quasi-field is present. The dashed green lines 1, 2 and 3 represent the transit-time limited responses with the contribution of the estimated potential (between 10 mV and 20 mV) generated by the doping grading.

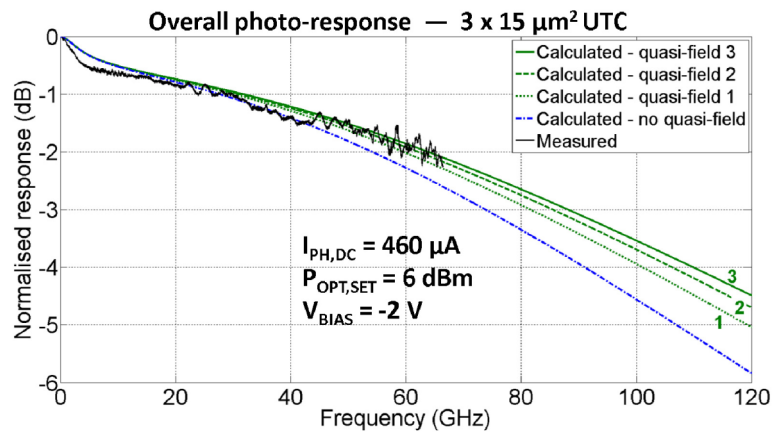


Fig. 14. Overall frequency response of the $3 \times 15 \mu\text{m}^2$ UTCs, for the diffusion only scenario (dotted blue line) and the three different quasi-field scenarios (dashed green lines) depicted in Fig. 13, compared with the measured response (continuous black line).

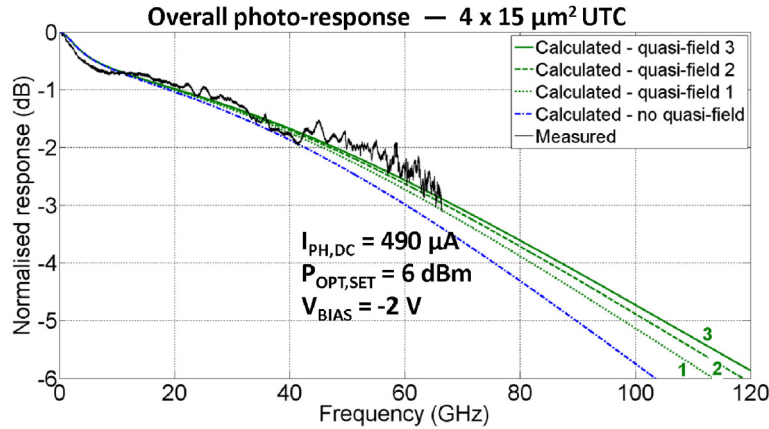


Fig. 15. Overall frequency response of the $4 \times 15 \mu\text{m}^2$ UTCs, for the diffusion only scenario (dotted blue line) and the three different quasi-field scenarios (dashed green lines) depicted in Fig. 13, compared with the measured response (continuous black line).

The agreement between Circuit 3 and measured results is good. In particular the results obtained by incorporating the transit-time limited response 2, which exhibited a 235 GHz 3 dB bandwidth, appears to provide a good agreement with the experimental data for both $3 \times 15 \mu\text{m}^2$ and $4 \times 15 \mu\text{m}^2$ UTCs. For the $3 \times 15 \mu\text{m}^2$ area device, the responses 1, 2 and 3 exhibit 3 dB bandwidth of 82 GHz, 86 GHz and 88 GHz respectively. For the $4 \times 15 \mu\text{m}^2$ area device, the responses 1, 2 and 3 exhibit 3 dB bandwidth of 65 GHz, 67 GHz and 69 GHz respectively.

4. Conclusions

Design of optimised antennas for integration with UTCs requires accurate knowledge of the complex UTC source impedance in order to achieve maximum radiated power.

The maximisation of the power extracted from a UTC is central to the successful realisation of a photonic millimetre-wave emitter. When the UTCs are integrated with antennas, such maximisation entails the optimisation of the energy coupling between UTC and antenna. Accurate knowledge of the UTC complex impedance over the frequency range is essential to maximise the power coupled from the UTC to the antenna, by realising complex-conjugate impedance matching. This aspect of antenna integrated UTCs has not received much attention in the literature. In this paper we have carried out a semi-analytical investigation of the impedance of waveguide UTCs, supported by experimental data taken up to 110 GHz and circuit analysis. The results we have shown can be employed to design antennas with an optimised complex impedance within the frequency range of interest. With regard to the UTC design, our analysis has pointed out an aspect on which further research effort can be focused.

The new circuit model we have introduced is applicable up to frequencies at which the device dimensions become significant relative to the effective wavelength. For the analysis we have presented, the model is successfully applied up to 110 GHz, where the effective wavelength is about 70 times greater than the UTC length. The lumped element analysis can be employed up to about 400 GHz, where the effective wavelength is 20 times the UTC length; however, to validate the model up to such frequencies, the support of 3D full-wave modelling of the whole UTC structure will be needed. Above 400 GHz the lumped element analysis is expected gradually to lose validity.